# UNIVERSITY OF ARKANSAS

## Introduction to Scientific Computing with Applications

Tulin Kaman

Computational Applied Mathematics Research Group
Department of Mathematical Sciences
University of Arkansas, Fayetteville
`https://kaman.uark.edu/`

DEPARTMENT OF INDUSTRIAL ENGINEERING
STUDENT CHAPTER of INFORMS SEMINAR

February 9, 2024

- Scientific computing is a discipline concerned with the development and study of **numerical algorithms** for solving mathematical problems that arise in various disciplines in science and engineering.

- The starting point is a given mathematical model which has been formulated in an attempt to explain and understand an observed phenomenon
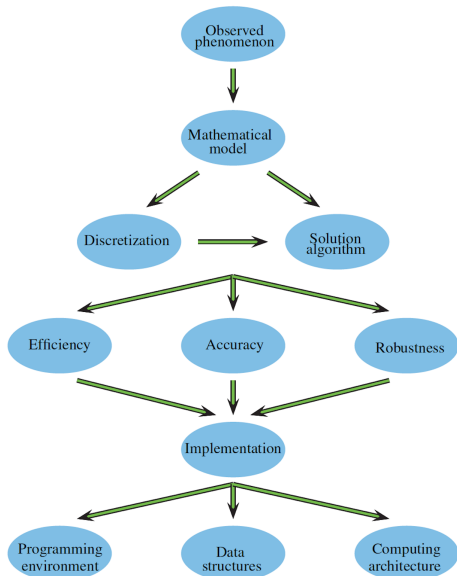
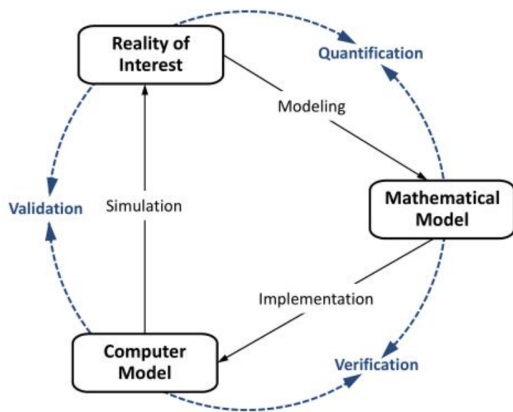# Terminology: Uncertainty Quantification, Validation & Verification studies



Figure: Terminology for Model Credibility. S. Schlesinger, 1979.

# Applications: I

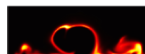"Verification and Validation study of Large Eddy Simulations of turbulent mixing and combustion within the engine of a scramjet", in collaboration with Stanford University's Predictive Science Academic Alliance Program
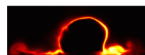
X. Gong, Y. Xu, V. Mahadeo, TK, J. Larsson and J. Glimm. Discrete and Continuous Dynamical Systems, 36(8), pp. 4383 – 4402, 2016.
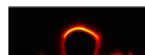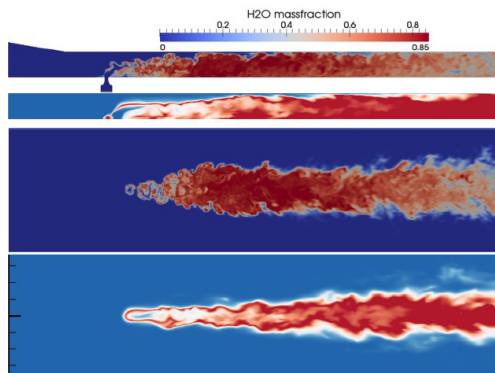


(A) x/h = 5

(B) x/h = 7

(C) x/h = 9
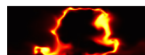
(D) x/h = 11
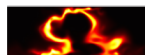
(E) x/h = 13
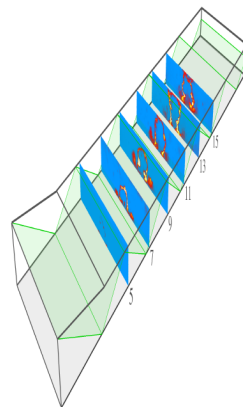
# Applications: II

*Paul Scherrer Institute, ETH-Zurich, University of Zurich*, Switzerland
(2013-2017).
"Realistic Injection Simulations of a Cyclotron Spiral Inflector using OPAL", in
collaboration with Department of Physics MIT

D.Winklehner, A. Adelmann, A. Gsell, TK and D. Campo.124201 Phys. Rev. Accel. Beams, Volume 20(12), pp.124201, 2017.
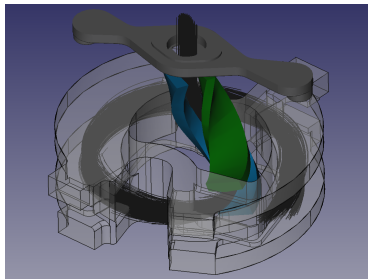


Investigate the space charge components in spiral inflector to determine the limits of
IsoDAR Cyclotron which accelerates a 5 mA beam of $H2+$ molecules up to the final
energy of 60 MeV.

# Applications: III

"Statistical Learning for Nonlinear Dynamical Systems with Applications to Aircraft-UAV Collisions", in collaboration with University of Arkansas Department of Industrial Engineering,

X. Liu, X. Liu, TK, X. Lu and G. Lin, Technometrics, pp. 1 – 21, 2023.
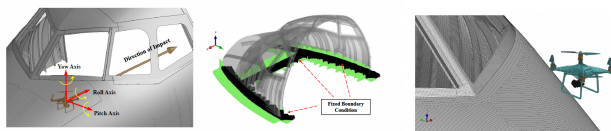


Consider the Aircraft (nose) metal skin deformation process due to UAV collisions at different impact attitudes (i.e., pitch degree, yaw degree and roll degree)

We wish to believe that the numerical results of a computer calculation, especially those obtained as output of a software package, contain no error – at least not a significant or intolerable one. But careless numerical computing does occasionally lead to trouble.



- The Patriot Missile failure, in Dharan, Saudi Arabia, on February 25, 1991 which resulted in 28 deaths, is ultimately attributable to poor handling of rounding errors.

- The explosion of the Ariane 5 rocket just after lift-off on its maiden voyage off French Guiana, on June 4, 1996, was ultimately the consequence of a simple overflow.

- The sinking of the Sleipner A offshore platform in Gandsfjorden near Stavanger, Norway, on August 23, 1991, resulted in a loss of nearly one billion dollars. It was found to be the result of inaccurate finite element analysis.

`https://www.ima.umn.edu/~arnold/disasters/disasters.html`

# Numerical algorithms and errors

The types of error that may limit the accuracy of a numerical calculation:

1. Errors in the problem to be solved.
   - Errors in the mathematical model
   - Errors in the input data
2. Approximation errors
   - Discretization errors
   - Convergence errors
3. Roundoff errors
   - arise because of the finite precision representation of real numbers

# Discretization errors in action I

An example that illustrates the behavior of discretization errors.
**Example:** Approximate the derivative $f'(x_0)$ of a given smooth function $f(x)$ at the point $x = x_0$.

Consider a situation where $f(x)$ may be evaluated at any point $x$ near $x_0$, but

- $f'(x_0)$ may not be directly available
- or is computationally expensive to evaluate

$\Rightarrow$ approximate $f'(x_0)$ by evaluating $f$ at $x$ near $x_0$.

**Theorem: Taylor's series.** Assume that $f(x)$ has $k+1$ derivatives in an interval containing the points $x_0$ and $x_0 + h$. Then

$$f(x_0+h) = f(x_0) + hf'(x_0) + \frac{h^2}{2!}f''(x_0) + \cdots + \frac{h^k}{k!}f^{(k)}(x_0) + \frac{h^{k+1}}{(k+1)!}f^{(k_1)}(\xi)$$

where $\xi$ is some point between $x_0$ and $x_0 + h$.

## Discretization errors in action II

The *algorithm* for approximating $f'(x_0)$ is to calculate

$$f'(x_0) \approx \frac{f(x_0 + h) - f(x_0)}{h}$$

The approximation has the *discretization error*

$$\left| f'(x_0) - \frac{f(x_0 + h) - f(x_0)}{h} \right| = \left| \frac{h}{2} f''(x_0) + \frac{h^2}{6} f'''(x_0) + \frac{h^3}{24} f^{(4)}(x_0) + ... \right|$$

Geometrically, the tangent $f'(x_0)$ is approximated by the chord

$$\frac{f(x_0 + h) - f(x_0)}{h}$$
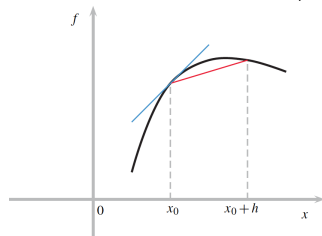


$$\left| f'(x_0) - \frac{f(x_0 + h) - f(x_0)}{h} \right| = \frac{h}{2} \left| f''(\xi) \right|, \qquad \text{where } x_0 < \xi < x_0 + h$$

**Example:** Let $f(x) = \sin(x)$ be defined on the real line $-\infty < x < \infty$ and set $x_0 = 1.2$ Thus, $f(x_0) = \sin(1.2) \approx 0.932....$

- The exact value:
  $f'(x_0) = \cos(1.2) = 0.362357754476674...$

- For $h = 0.1$, the approximation
  $f'(x_0) \approx (\sin(1.3) - \sin(1.2))/0.1 = 0.315...,$
  which is not very accurate.

| $h$ | Absolute error |
|------|----------------|
| 0.1 | 4.716676e-2 |
| 0.01 | 4.666196e-3 |
| 0.001 | 4.660799e-4 |
| 1.e-4 | 4.660256e-5 |
| 1.e-7 | 4.619326e-8 |

- The error appears to decrease like $h$. Using the knowledge of
  $f''(x) = -\sin(x) \Rightarrow f''(1.2)/2 \approx -0.466$
  The quantity $0.466h$ provides an accurate estimate for the absolute error values.

# The combined effect of discretization and roundoff errors.

| $h$ | Absolute error |
|---|---|
| 1.e-8 | 4.361050e-10 |
| 1.e-9 | 5.594726e-8 |
| 1.e-10 | 1.669696e-7 |
| 1.e-11 | 7.938531e-6 |
| 1.e-13 | 4.250484e-4 |
| 1.e-15 | 8.173146e-2 |
| 1.e-16 | 3.623578e-1 |
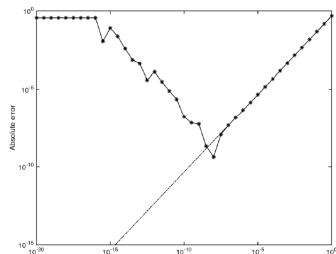


When $h$ gets below approximately $10^{-8}$ the discretization error becomes very small and roundoff error starts to dominate.

# Simulations and Modeling of Turbulent Mixing

**Rayleigh–Taylor Instability (RTI):**

arises at the interface between two fluids of different densities whenever the pressure gradient opposes the density gradient.

**Richtmyer-Meshkov Instability (RMI):**

arises when a shock wave interacts with the interface. RMI is known as the impulsive or shock-induced RTI.



Photograph courtesy of NASA, ESA, J. Hester and A. Loll (ASU)
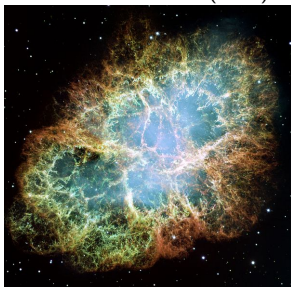


Photograph courtesy of David Jewitt, University of California at Los Angeles.
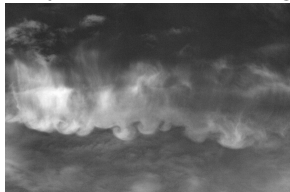
# Problem statement

- Growth rate of RTI, $\boxed{\alpha_{RTI}}$,

$$h = \alpha A g t^2$$

  $h$, penetration distance of the light fluid into the heavy fluid
  $A$, Atwood ratio $= (\rho_1 - \rho_2)/(\rho_1 + \rho_2)$
  $g$, acceleration

- Growth rate of RMI, $\boxed{V_{RMI}}$,

$$V_{RMI} = k h_0 A \Delta U$$

  $k$, wave number
  $h_0$, initial perturbation
  $A$, Atwood ratio $= (\rho_1 - \rho_2)/(\rho_1 + \rho_2)$
  $\Delta U$, interface velocity
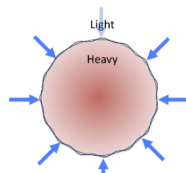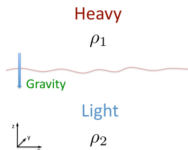
# Numerical Approaches to Model Turbulent Flows

Three levels of numerical simulation for turbulent flows:

- Direct Numerical Simulation (DNS)
    - The full NSE is solved without any model for turbulence
    - The most demanding method among the three, very accurate, but limited to moderate Reynolds numbers and simplified geometries
- Large Eddy Simulation (LES)
    - Flow field is resolved down to a certain length scale, and scales smaller than that are modeled rather than resolved
    - Computational cost higher than RANS, but much lower than DNS
- Reynolds Averaged Navier Stokes (RANS)
    - Time-averaged equations solving for the mean values of all quantities
    - The least demanding in terms of resources

Front Tracking (FT), to achieve resolution of steep and sharp density gradients

# Front Tracking API

For the numerical simulations of multiphase flows, one of the advantages of front tracking method is in dealing with the contact discontinuities.
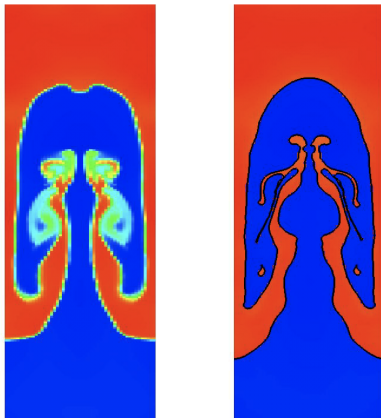


Figure: RTI single mode simulation at t = 10s. Comparison of a FLASH run without (left) and with (right) the use of front tracking API.

# Model: Compressible Navier-Stokes

The governing equations of motion for viscous turbulent flows are the three-dimensional (3D) compressible Navier-Stokes equations.
The conservation laws of continuity, momentum and energy

$$\frac{\partial \rho}{\partial t} + \frac{\partial(\rho v_i)}{\partial x_i} = 0 \ , \tag{1}$$

$$\frac{\partial \rho v_j}{\partial t} + \frac{\partial(\rho v_i v_j + p\delta_{ij} - d_{ij})}{\partial x_i} = 0 \ , \tag{2}$$

$$\frac{\partial E}{\partial t} + \frac{\partial((E+p)v_i - d_{ij}v_j + q_i)}{\partial x_i} = 0 \ , \tag{3}$$

where $\rho, v_i, p$ and $E$ are the density, velocity in $i$ direction, pressure and the total energy respectively. Any repeated index in a single term is summed over the spatial index (i=1,2,3 for 3D). The viscous stress tensor, $d_{ij}$, in terms of dynamic viscosity $\mu$ is

$$d_{ij} = \mu \left( \left( \frac{\partial v_i}{\partial x_j} + \frac{\partial v_j}{\partial x_i} \right) - \frac{2}{3} \frac{\partial v_k}{\partial x_k} \delta_{ij} \right) \ , \tag{4}$$

The heat-flux calculated by Fourier's law: $q_i = -k \frac{\partial T}{\partial x_i}$
$T$: temperature, $k$: thermal diffusion coefficient

# Model: Compressible Euler Equations

The equations 5- 7 are the compressible Euler equations for inviscid flows where the viscosity and heat conduction are neglected.

$$\frac{\partial \rho}{\partial t} + \frac{\partial (\rho v_i)}{\partial x_i} = 0 \ , \tag{5}$$

$$\frac{\partial \rho v_j}{\partial t} + \frac{\partial (\rho v_i v_j + p \delta_{ij})}{\partial x_i} = 0 \ , \tag{6}$$

$$\frac{\partial E}{\partial t} + \frac{\partial ((E + p) v_i)}{\partial x_i} = 0 \ , \tag{7}$$

The Euler equations are extended with the mass fraction equation for cases with binary fluid mixing

$$\frac{\partial \rho Y_j}{\partial t} + \frac{\partial (\rho v_i Y_j(}{\partial x_i} = 0, \tag{8}$$

where $Y_j$ is the mass fraction for fluid $j = 1, 2$.

# Equation of State (EOS)

- A thermodynamic equation relating state variables which describing the properties of fluids.
- General form: A system in thermodynamic equilibrium can be completely described by the basic thermodynamic variables pressure $p$ and specific volume $V$. A family of states in thermodynamic equilibrium may be described by a curve in the $p - v$ plane, each characterised by a particular value of a variable temperature $T$.

$$f(p, V, T) = 0$$

$$T = T(p, V), p = p(T, V), V = V(T, p)$$

- Classical ideal gas law; $pV = nRT$
- Van der Waals (cubic function of $V_m$: molar volume, $V/n$) EOS
- Helmholtz (multiparameter) EOS
- Stiffened (water under high pressures, underwater nuclear explosions)

$$p = (\gamma - 1)\rho e - p^*$$

where the internal energy

$$e = \frac{C_p}{\gamma} T + \frac{p^*}{\gamma \rho}$$

# Numerical Algorithms:

Reconstruction-evolution or shock-capturing methods (Laney, 1998; LeVeque, 2002) are the methods used to simulate compressible turbulent mixing.

The upwind methods: (upstream variables are used to calculate the derivatives in a flow field)

- higher-order Godunov methods
- the Van Leer method,
- the piecewise-parabolic method (PPM)
- essentially non-oscillatory (ENO) methods
- weighted essentially non-oscillatory (WENO) methods

These methods treat the flux using either a Riemann solver or by flux-splitting.

Their nonlinear implicit dissipation mechanisms require very high spatial resolutions to minimize numerical diffusion.

# Upwind methods

- Utilise the direction of wave propagation emboided in the PDEs to construct the numerical algorithms.
- The CIR method (first-order upwind scheme): Courant, Isaacson, and Rees

**1D advection equation $u_t + au_x = 0$**

describes a wave propagating along x-axis with velocity $a$. Use upstream variables to calculate the spatial derivative $\partial u / \partial x$.

There are two directions at point $i$.

① If $a > 0$, the traveling wave solution propagates towards the right,
- the left side of $i$: upwind side
- the right side : downwind side.

$$\frac{u_i^{n+1} - u_i^n}{\Delta t} + a\frac{u_i^n - u_{i-1}^n}{\Delta x} = 0$$

② If $a < 0$, the traveling wave solution propagates towards the left,
- the left side of $i$: downwind side
- the right side: upwind side.

$$\frac{u_i^{n+1} - u_i^n}{\Delta t} + a\frac{u_{i+1}^n - u_i^n}{\Delta x} = 0$$

# Simple case: Weighted essentially non-oscillatory (WENO) Method I

Solve $u_t + f(u)_x = 0$

Approximate the spatial derivative using WENO $L(u) \approx -f(u)_x$ and use a time stepping method to solve the system.

High order accurate and non-oscillatory scheme flux reconstruction uses a convex combination of $k$ candidate stencils. For $k = 3$, the fifth $(2k - 1)$ order finite difference WENO schemes approximates the derivative $f(u)_x$ at a point $x_i$,

$$f(u)_x|_{x=x_i} \approx \frac{1}{\Delta x}(\hat{f}_{i+1/2} - \hat{f}_{i-1/2}) \tag{9}$$

where $u$ is the state vector, $f(u)$ is the flux, $\hat{f}_{i+1/2}$ and $\hat{f}_{i-1/2}$ are the fluxes at the cell boundaries, and $\hat{f}^+_{i+1/2}, \hat{f}^-_{i+1/2}$ are the positive and negative parts of

$$\hat{f}_{i+1/2} = \hat{f}^+_{i+1/2} + \hat{f}^-_{i+1/2}.$$

# Simple case: Weighted essentially non-oscillatory (WENO) Method II

The fifth order WENO scheme uses three stencils

$$\hat{f}_{i+1/2} = \sum_{j=1}^{3} \omega_i \hat{f}_{i+1/2}^{(j)}$$

with three third order fluxes $\hat{f}_{i+1/2}^{(j)}$ and the nonlinear weights $\omega_i$.

- To calculate the fluxes $\hat{f}_{i+1/2}^{+}$ and $\hat{f}_{i+1/2}^{-}$, calculate the smoothness measurements to determine if a shocks lies with the stencil.

$$\hat{f}_{i+1/2}^{+} = w_0^{+}\left(\frac{2}{6}f_{i-2}^{+} - \frac{7}{6}f_{i-1}^{+} + \frac{11}{6}f_i^{+}\right) + w_1^{+}\left(-\frac{1}{6}f_{i-1}^{+} + \frac{5}{6}f_i^{+} + \frac{2}{6}f_{i+1}^{+}\right) + w_2^{+}\left(\frac{2}{6}f_i^{+} + \frac{5}{6}f_{i+1}^{+} - \frac{1}{6}f_{i+2}^{+}\right)$$

$$\hat{f}_{j+1/2}^{-} = w_0^{-}\left(-\frac{1}{6}f_{i-1}^{-} + \frac{5}{6}f_i^{-} + \frac{2}{6}f_{i+1}^{-}\right) + w_1^{-}\left(\frac{2}{6}f_i^{-} + \frac{5}{6}f_{i+1}^{-} - \frac{1}{6}f_{i+2}^{-}\right) + w_2^{-}\left(\frac{11}{6}f_{i+1}^{-} - \frac{7}{6}f_{i+2}^{-} - \frac{2}{6}f_{i+3}^{-}\right)$$

$$f^{+}(u)_x \approx \frac{1}{\Delta x}\left(\hat{f}_{i+1/2}^{+} - \hat{f}_{i-1/2}^{+}\right)$$

$$f^{-}(u)_x \approx \frac{1}{\Delta x}\left(\hat{f}_{i+1/2}^{-} - \hat{f}_{i-1/2}^{-}\right)$$

# Weighted essentially non-oscillatory (WENO) Method

flux-averaged WENO method uses local Lax-Friedrichs flux-splitting and a characteristic decomposition of the variables and fluxes (Schilling and Latini, 2004)

1. compute the average state $\overline{\varphi}^\alpha$ at $(i+1/2, j, k)$ using a Roe average;

2. evaluate the left and right eigenvector matrices $L(\overline{\varphi})$ and $R(\overline{\varphi})$, and the eigenvalues of the Jacobian matrix at the average state;

3. for every stencil, project the conservative fields and the fluxes onto the local characteristic directions using the left eigenvector matrix ($2r-1$ is the formal order of accuracy), $\varphi_{m,j,k}^{\alpha(ch)} = L(\overline{\varphi})\varphi_{m,j,k}^\alpha$ and $F_{m,j,k}^{\alpha(ch)} = L(\overline{\varphi})F_{m,j,k}^\alpha$ with $m \in [i-r+1, i+r]$;

4. evaluate the left and right characteristic fluxes $\hat{F}_{m,j,k}^{\alpha(ch)^\pm}$ pointwise value $F_{m,j,k}^\alpha$ using local or global Lax-Friedrichs flux-splitting;

5. reconstruct the numerical characteristic flux functions $\hat{F}_{m,j,k}^{\alpha(ch)^\pm}$ from the pointwise values $F_{m,j,k}^\alpha$ using the WENO method

6. compute the numerical flux function in physical space by projecting back using the right eigenvector matrix $F_{i+1/2,j,k}^\alpha = R(\overline{\varphi})(F_{i+1/2,j,k}^{\alpha,+} + F_{i+1/2,j,k}^{\alpha,-})$

7. obtain the fluxes in the y- and z-directions $(i, j+1/2, k)$ and $(i, j, k+1/2)$

8. advance the solution using the second-order Runge-Kutta scheme,

# Problem 1: Sod's Shock Tube Problem

For the contact discontinuity tracking,
Sod's shock tube problem which is a Riemann problem with initial condition

$$(\rho, u, p) = \begin{cases} (1, 0, 1) & \text{if } -5 \le x \le 0 \\ (0.125, 0, 0.1) & \text{if } 0 \le x \le 5 \end{cases} \tag{10}$$
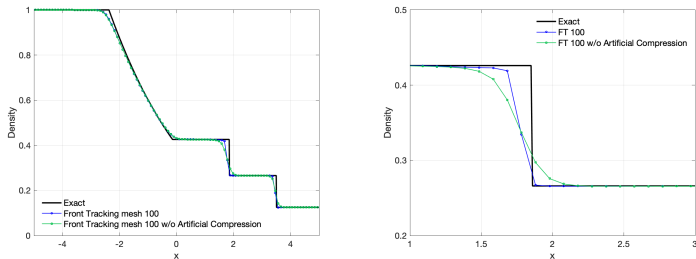


Figure: Left: The fifth order WENO scheme with and without artificial compression method of Yang are compared with the exact solution of Sod's shock tube problem. Right: A zoomed view on domain [1,3].

# Problem 2: Shock-entropy wave interaction (Shu-Osher)

Study the stability and accuracy of the WENO scheme for strong shocks.
Shu-Osher's test problem corresponds to a Mach $M = 3$ shock wave passing
through an entropy wave on the spatial domain $(-5, 5)$ and the time domain
$(0, 2)$.

$$(\rho, u, p) = \begin{cases} (3.857143, 2.629369, 10.33333) & \text{if } x \leq -4 \\ (1 + 0.2 \sin 5x, 0, 1) & \text{if } x \geq -4 \end{cases} \tag{11}$$

The solution near N-wave ($[-2, 0]$,) the transition to the N-wave ($x \in [0, 1]$),
the entropy wave ($x \in [1, 2]$), and the shock ($x \in [2, 2.5]$) is displayed under
three levels of mesh refinement, 200, 400 and 1600 mesh points at $t = 1.8$.
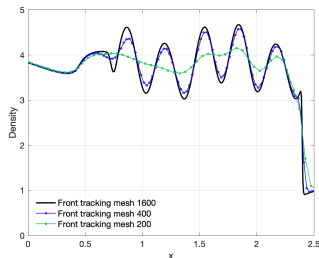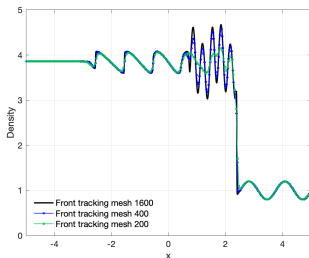
# Problem 3: Single-Mode Richtmyer-Meshkov Instability I

1. Set RMI simulations according to Collins and Jacobs 2002 shock tube experiments for Mach numbers $M = 1.11$ and $M = 1.21$.



(a)
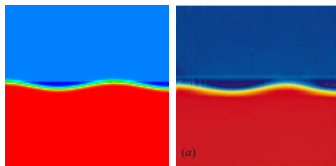
- The light fluid (air) at the top and heavy fluid ($SF_6$) at the bottom.
- The shock tube *test* section: W X L : 8.9 cm x 75 cm.
- The initial density profile over the diffuse interface is set by
  $\rho(y) = \bar{\rho}\left(1 + A \; erf\left(\frac{\sqrt{\pi}y}{\delta}\right)\right)$ where $\bar{\rho} = (\rho_1 + \rho_2)/2$ average density.
- The diffuse interface thickness is 0.5 cm between the two fluids.
- The location of the initial shock ($y = 1$ cm) and the perturbed interface ($y = 3$ cm). Latini, Schilling and Don 2007 studies. *JCP*, 221(2), 2007; *PoF*, 19(2), 2007.
- Quantities of interest: amplitude and displacement measurements

# The parameter values of RMI simulations

| | Mach Numbers | |
|---|---|---|
| | 1.11 | 1.21 |
| Initial amplitude $a_0$ (cm) | 0.229 | 0.183 |
| Initial wavelength $\lambda_0$ (cm) | 5.933 | |
| Ratio between $a_0/\lambda_0$ | 0.0386 | 0.0308 |
| Heavy fluid ($SF_6$) density $\rho_1$ (g/cm$^3$) | $5.944 \times 10^{-3}$ | |
| Light fluid (air-acetone) density $\rho_2$ (g/cm$^3$) | $1.351 \times 10^{-3}$ | |
| Atwood number $A$ | 0.6053 | |
| Molecular weight of $SF_6$ (g/mol) | 146.05 | |
| Molecular weight of air-acetone (g/mol) | 34.76 | |
| Ratio of specific heats $\gamma$ | 1.276 | |
| Pressure at interface $p$ (bar) | 0.956 | |
| Courant–Friedrichs–Lewy (CFL) number | 0.45 | |

The boundary conditions

- Streamwise direction (inflow and reflection)
- Spanwise direction (periodic)

# Validation: Comparison between simulations and experiments

Comparison of the amplitude between Collins and Jacobs 2002 experiments and FronTier simulations for M = 1.21
The number of grid points per initial perturbation wavelength is 64, 128 and 256 for the coarse, medium and fine grid simulations.
Finest grid: 512 cells per initial wavelength
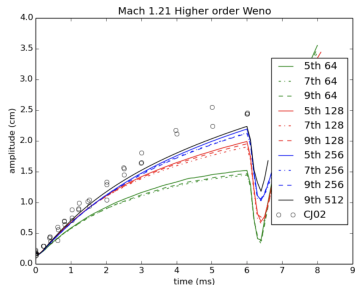
Top: The density profile of the fine grid simulation at times 6; 6:2 and 6:4 ms.
Bottom: Experimental PLIF images at times 6.006; 7.005 and 7.781 ms.
The experimental images are taken from Figure 6 of Collins and Jacobs (reprinted with the per- mission of Cambridge University Press)
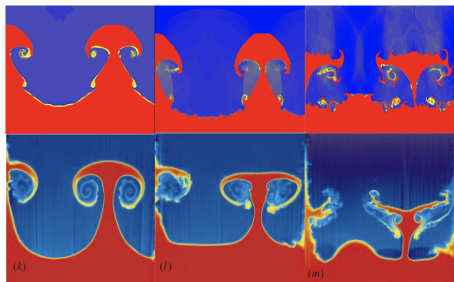
# Model: Reactive Compressible Naiver-Stokes Equation

$$\frac{\partial \rho}{\partial t} + \frac{\partial}{\partial x_j}\left(\rho v_j\right) = 0 \; , \tag{12}$$

$$\frac{\partial}{\partial t}\left(\rho v_i\right) + \frac{\partial}{\partial x_j}\left(\rho v_i v_j\right) + \frac{\partial p}{\partial x_i} = \frac{\partial d_{ij}}{\partial x_j} \; , \tag{13}$$

$$\frac{\partial E}{\partial t} + \frac{\partial \left[(E + p) v_j\right]}{\partial x_j} = \frac{\partial}{\partial x_j}\left(d_{ij} v_i\right) - \frac{\partial q_j}{\partial x_j} + H \; , \tag{14}$$

$$\frac{\partial}{\partial t}\left(\rho Y_i\right) + \frac{\partial}{\partial x_j}\left(\rho v_j Y_i\right) = \nabla \cdot \rho d_j \nabla Y_i + \dot{m}_i \; , \tag{15}$$

$Y_i$: mass fraction of species $i$, $\dot{m}_i$: production rate of species $i$
$H$: total heat release rate from the chemical reactions
Viscous stress tensor

$$d_{ij} = 2\mu S_{ij}^* = \mu \left[\left(\frac{\partial u_i}{\partial x_j} + \frac{\partial u_j}{\partial x_i}\right) - \frac{2}{3}\delta_{ij}\frac{\partial u_k}{\partial x_k}\right] \; , \tag{16}$$

The heat-flux

$$q = -k\nabla T \; . \tag{17}$$

# Dynamic viscosities and thermal conductivities I

for single gas species

$$\mu_i = 2.6693 \cdot 10^{-5} \frac{\sqrt{M_i T}}{\delta_i^2 \Omega_{ij}^{(2,2)}}$$

$$k_i = \mu_i \left( c_{p,i} + \frac{5}{4} \frac{R}{M_i} \right)$$

$M_i$: molecular mass of species $i$
$\delta_i$: collison diameter
$\Omega_{ij}$: collision integral for viscosity

for a mixture, based on averages of the individual species properties. Semi-empirical mixture rules[*]

$$\mu = \sum_{i=1}^{N} \frac{Y_i \mu_i}{\triangle_i} \ , \qquad k = \sum_{i=1}^{N} \frac{Y_i k_i}{\triangle_i} \ ,$$

of the mixture, where

$$\triangle_i = \sum_{j=1, j \neq i}^{n} G_{ij} \frac{M_i}{M_j} Y_j \ .$$

$$G_{ij} = \frac{1}{\sqrt{8}} \left( 1 + \frac{M_i}{M_j} \right)^{-1/2} \left[ 1 + \left( \frac{\mu_i}{\mu_j} \right)^{-1/2} \left( \frac{M_i}{M_j} \right)^{1/4} \right]^2 \ .$$

[*] R. S. Brokaw, Viscosity of Gas Mixtures, vol. 4496, National Aeronautics and Space Administration, 1968.

- NASA provides tables of coefficients[(*)] . $C_P(T), H(T), S(T)$ for individual species are calculated based on the NASA polynomials.

$$\frac{C_P(T)}{R} = a_1 + a_2 T + a_3 T^2 + a_4 T^3 + a_5 T^4,$$

$$\frac{H(T)}{RT} = a_1 + a_2 \frac{T}{2} + a_3 \frac{T^2}{3} + a_4 \frac{T^3}{4} + a_5 \frac{T^4}{5} + \frac{a_6}{T}$$

$$\frac{S(T)}{R} = a_1 ln(T) + a_2 T + a_3 \frac{T^2}{2} + a_4 \frac{T^3}{3} + a_5 \frac{T^4}{4} + a_7.$$

To improve the table accuracy, the temperature range is divided into the lower part, from 300 K to 1000 K, and the higher part, from 1000 K to 5000 K.

- Find the temperature $T$ for the chemistry calculation. This is done using a nonlinear equation solver, which is derived using the expressions

$$\frac{RT}{M} = \frac{P}{\rho} = (\gamma(T) - 1)E = \left( \frac{C_P}{C_P - R/M} - 1 \right) E$$

$$\left( a_1 + a_2 T + a_3 T^2 + a_4 T^3 + a_5 T^4 - 1/M \right) RT = E$$

[(*)]B. J. McBride, S. Gordon, and M. A. Reno 1993.

# General Reaction Rate Model I

- The production rates $\dot{m}_i$

$$\dot{m}_i = \sum_{j=1}^{N} M_i v_{ji} r_j \ , \tag{18}$$

$N$: number of reactions
$M_i$: molecular mass of species $i$
$r_j$: release rate for reaction $j$
$v_{ji}$: stoichiometric coefficient of species $i$ in the reaction $j$.

- The total heat release rate $H$

$$H = \sum_{j=1}^{N} \sum_{i=1}^{n} h_i M_i v_{ji} r_j \ , \tag{19}$$

$n$: number of species
$h_i$: enthalpy of species $i$

# General Reaction Rate Model II

The reaction rate $r_j$

$$r_j = k_{fj} \prod_{i=1}^{n} \left( \frac{\rho Y_i}{M_i} \right)^{v_{ji}} - k_{bj} \prod_{i=1}^{n} \left( \frac{\rho Y_i}{M_i} \right)^{v_{ji}''}.$$

$k_{fj}$ and $k_{bj}$: forward and backward (reverse) rate coefficients
$Y_i$ and $M_i$: mass fraction and the molecular weight of the species $i$
$v_{ji}$ and $v_{ji}''$: reaction $j$'s stoichiometric coefficients of species $i$ on the reactant and product side.
The two rate coefficients are computed by the empirical Arrhenius law.

$$k_{fj} = A_j T^{n_j} \exp \left( \frac{-E_j}{RT} \right) \, ,$$

$A_j$, $n_j$ and $E_j$ are the pre-exponential constant, the temperature exponent, and the activation energy of reaction $j$.

$$k_{bj} = \frac{k_{fj}}{\left( \frac{P_a}{RT} \right)^{\sum\limits_{i=1}^{n} v_{ji}} \exp \left( \frac{\Delta S_j}{R} - \frac{\Delta H_j}{RT} \right)}$$

# Detailed/Reduced Chemical Mechanism

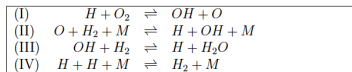## Detailed Chemical Mechanism

- There are eight reacting species involved:
  $H_2$; $O_2$; $H_2O$; $H$; $O$; $OH$; $HO_2$ and $H_2O_2$

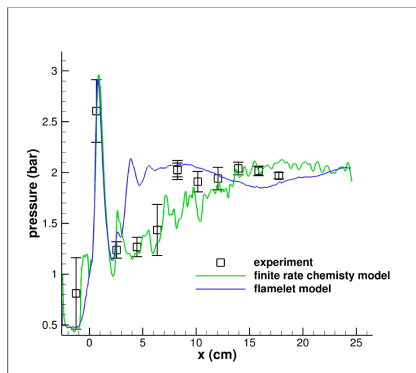| Reaction | | $A$ | $n$ | $E$ |
|---|---|---|---|---|
| **Hydrogen-oxygen chain** | | | | |
| $1.H + O_2 \rightarrow OH + O$ | | $3.52 \times 10^{16}$ | -0.7 | 71.4 |
| $2.H_2 + O \rightarrow OH + H$ | | $5.06 \times 10^4$ | 2.7 | 26.3 |
| $3.H_2 + OH \rightarrow H_2O + H$ | | $1.17 \times 10^9$ | 1.3 | 15.2 |
| $4.H_2O + O \rightarrow OH + OH$ | | $7.60 \times 10^0$ | 3.8 | 53.4 |
| **Direct recombination** | | | | |
| $5^a.H + H + M \rightarrow H_2 + M$ | | $1.30 \times 10^{18}$ | -1.0 | 0.0 |
| $6^a.H + OH + M \rightarrow H_2O + M$ | | $4 \times 10^{22}$ | -2.0 | 0.0 |
| $7^a.O + O + M \rightarrow O_2 + M$ | | $6.17 \times 10^{15}$ | -0.5 | 0.0 |
| $8^a.H + O + M \rightarrow OH + M$ | | $4.71 \times 10^{18}$ | -1.0 | 0.0 |
| $9^a.O + OH + M \rightarrow HO_2 + M$ | | $8.00 \times 10^{15}$ | 0.0 | 0.0 |
| **Hydroperoxyl reactions** | | | | |
| $10^a.H + O_2 + M \rightarrow HO_2 + M$ | $k_0$ | $5.75 \times 10^{19}$ | -1.4 | 0.0 |
| | $k_\infty$ | $4.65 \times 10^{12}$ | 0.4 | 0.0 |
| $11.HO_2 + H \rightarrow OH + OH$ | | $7.08 \times 10^{13}$ | 0.0 | 1.2 |
| $12.HO_2 + H \rightarrow H_2 + O_2$ | | $1.66 \times 10^{13}$ | 0.0 | 3.4 |
| $13.HO_2 + H \rightarrow H_2O + O$ | | $3.10 \times 10^{13}$ | 0.0 | 7.2 |
| $14.HO_2 + O \rightarrow OH + O_2$ | | $2.00 \times 10^{13}$ | 0.0 | 0.0 |
| $15.HO_2 + OH \rightarrow H_2O + O_2$ | | $2.89 \times 10^{13}$ | 0.0 | -2.1 |
| **Hydrogen peroxide reactions** | | | | |
| $16^b.OH + OH + M \rightarrow H_2O_2 + M$ | $k_0$ | $2.30 \times 10^{18}$ | -0.9 | -7.1 |
| | $k_\infty$ | $7.40 \times 10^{13}$ | -0.4 | 0.0 |
| $17.HO_2 + HO_2 \rightarrow H_2O_2 + O_2$ | | $3.02 \times 10^{12}$ | 0.0 | 5.8 |
| $18.H_2O_2 + H \rightarrow HO_2 + H_2$ | | $4.79 \times 10^{13}$ | 0.0 | 33.33 |
| $19.H_2O_2 + H \rightarrow H_2O + OH$ | | $1.00 \times 10^{13}$ | 0.0 | 15.0 |
| $20.H_2O_2 + OH \rightarrow H_2O + HO_2$ | | $7.08 \times 10^{12}$ | 0.0 | 6.0 |
| $21.H_2O_2 + O \rightarrow HO_2 + OH$ | | $9.63 \times 10^6$ | 2.0 | 2.0 |

## Reduced Chemical Mechanism

- Chemical reduction aims at lowering the effective number of reactions and chemical species in the simulation. Objective: to reduce computational cost ($\approx 30\%$ total time cost on chemistry calculation in Scramjet simulation).

- A four-step reaction mechanism[*] for $H_2/O_2$ interactions has been successfully verified against the result of detailed chemistry

| (I) | $H + O_2$ | $\rightleftharpoons$ | $OH + O$ |
|---|---|---|---|
| (II) | $O + H_2 + M$ | $\rightleftharpoons$ | $H + OH + M$ |
| (III) | $OH + H_2$ | $\rightleftharpoons$ | $H + H_2O$ |
| (IV) | $H + H + M$ | $\rightleftharpoons$ | $H_2 + M$ |

[*]: P Boivin, C Jimenez, AL Sanchez, FA Williams "Four-step and three-step systematically reduced chemistry for wide-range H2-air combustion problems" 2013
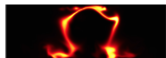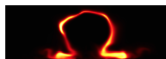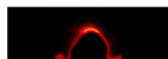
# Simulation Configuration

- Current grid resolution: 0.05 cm $\times$ 0.025 cm $\times$ 0.025 cm
- Modeling approach: fifth-order WENO based on finite volume + dynamic LES + finite rate chemistry model + reduced chemical mechanism.
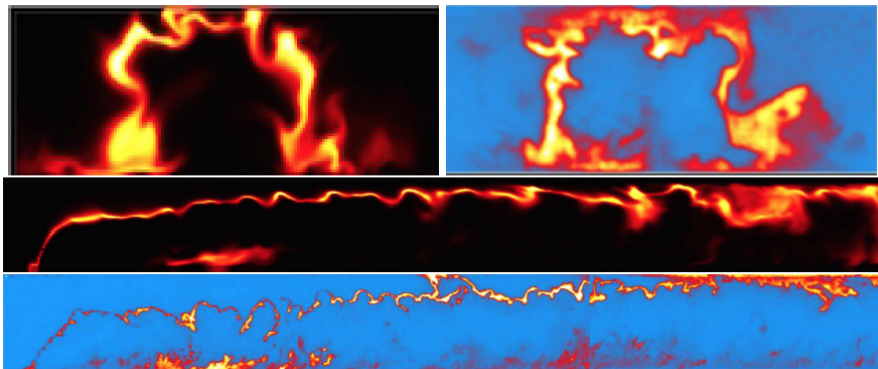
### Results - Pressure at Lower Wall

# Results - OH Mass Fraction



(A) x/h = 5

(B) x/h = 7

(C) x/h = 9

(D) x/h = 11

(E) x/h = 13
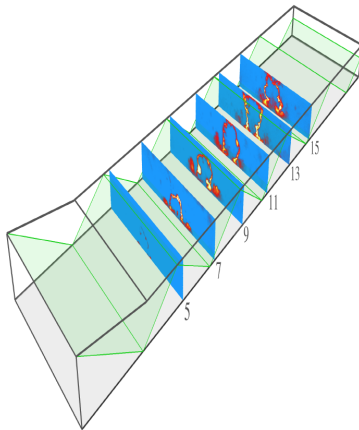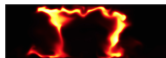
Mass fraction of OH in several end-view planes corresponding to the OH PLIF data (right frame) from experiment

OH mass fraction in several views, comparing finite rate chemistry simulation and by experiment. Top left frame (a)finite rate chemistry simulation, top right frame (b) experiment, both end views of the combustion chamber. Middle frame (c) finite rate chemistry simulation and bottom frame (d) experiment, a vertical cross section.

# Collaborators



- Dr. James Glimm (SBU) and Dr. Snezhana Abarzhi (UWA) for many helpful comments and discussions
- Dr. David Youngs (AWE) and Jeffrey W. Jacob (UofA) for providing their RTI and RMI experimental data
- Dr. Oleg Schilling (LLNL) for sharing RMI simulation data
- Dr. Ann Almgren (LBNL) for supporting new AMReX-FronTier development.
- Lawrence Jesser Toll Jr. Endowed Chair at the Department of Mathematical Sciences in the Fulbright College of Arts & Sciences, 2017-present.
- University of Arkansas Chancellor's Innovation Fund, 2022-2025. Arkansas High Performance Computing Center (AHPCC) for computational resources.
- NSF #2204490

# Kaman Computational Applied Mathematics Group



8th Annual Meeting of SIAM Central States Section Meeting, University of Nebraska-Lincoln, October 7-8, 2023.

- Irina Afanasyeva, Inflow Turbulence Generation Methods
- James Burton, Block-structured, adaptive mesh refinement
- Ryan Holley, Simulation of turbulent mixing due to Richtmyer-Meshkov Instability
- Xuan Gu, Efficient Physics-informed Neural Networks for solving PDEs
- Nailah Rawnaq, Generative adversarial network (GAN) for biomedical images
- Pritom Roy, Image Segmentation using U-NET CNN for biomedical images

# Association for Women in Mathematics (AWM) Student Chapter https://kaman.uark.edu/awm/



The Chapter is organized for educational and scientific purposes to promote:

- an increased knowledge of and greater interest in the mathematical sciences,
- a greater understanding of the contributions of women in the mathematical sciences; and
- mentoring and encouraging women and girls as they prepare for careers in the mathematical sciences.

# Society for Industrial and Applied Mathematics (SIAM) Student Chapter https://kaman.uark.edu/siam/



SIAM Student Chapter Spring 2024 Meeting, January 31, 2024

The Chapter is organized and operated for educational and scientific purposes:

- develop interactions among the students and faculty in sciences and engineering departments
- provide a learning environment to develop and improve students' skills in applied mathematics, computational science and engineering.

# 85th OK-AR MAA Section Meeting
https://maa.uark.edu/



85th Annual Meeting of OK-AR MAA Section

About    Hotel and Travel

**April 4-6, 2024 | University of Arkansas**

The Department of Mathematical Sciences at the University of Arkansas welcomes you to the 85th Annual OK-AR Mathematical Association of America Sectional Meeting on April 4th – 6th, 2024, to be held at the main campus of the University of Arkansas, in Fayetteville, AR.

Abstract submission deadline is March 5, 2024.

The registration will be available soon.

REGISTRATION          ABSTRACT SUBMISSION          SCHEDULE

**Plenary Speakers**

Edray Goins
Pomona College

Deanna Haunsperger
Carleton